Measurements of the foreign-broadened continuum of water vapor in the 6.3 μm band at −30 °C

Penny M. Rowe, Von P. Walden, and Stephen G. Warren

The foreign-broadened continuum of water vapor in the ν_2 band (5–7.7 μm, 1300–2000 cm^{-1}) is important for satellite-based retrievals of water vapor in the upper troposphere, where temperatures are below −25 °C. Continuum coefficients have previously been measured mostly at or above +23 °C. We present continuum coefficients in the ν_2 band retrieved from measurements made in Antarctica at temperatures near −30 °C: atmospheric transmission at South Pole Station and atmospheric emission at Dome C. The continuum coefficients derived from these measurements are generally in agreement with the widely used Mlawer, Tobin–Clough, Kneizys, Davies continuum. Differences are at most 30%, corresponding to a 6% relative error in retrieved upper-tropospheric humidity.

OCIS codes: 010.1320, 010.1280, 120.0280, 300.6340.

1. Introduction

Emission of infrared radiation by upper-tropospheric water vapor contributes significantly to the Earth's radiation budget, so climate monitoring requires accurate measurement of the water-vapor density in the upper troposphere. Remote sensing of the vertical distribution of water vapor requires accurate absorption coefficients for water vapor. Satellite-based remote sensing techniques traditionally retrieve upper-tropospheric humidity from measurements of infrared radiance in the ν_2 band between ~1300 and 2000 cm^{-1}. Soden *et al.*[1] found that radiation codes lacking the continuum overestimate the brightness temperature at the top of the atmosphere by ~1.7 K, resulting in a relative bias in retrieved upper-tropospheric humidity (pressure levels of 200–500 mbars)[1,2] of ~20%. In the upper troposphere the temperature ranges from −25° to −80 °C. At these temperatures, the water-vapor density is low enough that the self-broadened continuum contributes negligibly to the total continuum emission. Thus the foreign-broadened continuum of water vapor in the ν_2 band at temperatures below −25 °C is what is important for retrievals of upper-tropospheric humidity. In addition to its applicability to remote sensing, measurement of the water-vapor continuum at low temperatures provides constraints for theoretical work (e.g., that of Ma and Tipping[3]).

The continuum model used most often in atmospheric radiation codes is a version of the Clough, Kneizys, and Davies (CKD) continuum.[1,4] CKD fitted their foreign-broadened continuum to measurements by adjusting fit parameters. Some of the earliest measurements of water-vapor continuum coefficients were made by Burch and co-workers[5–7] at +23° to +155 °C. Their measurements were similar over this large temperature range, so the CKD foreign-broadened continuum was assumed to have no temperature dependence. The CKD continuum has been updated as more experimental results have become available, but the foreign-broadened portion does not currently include a dependence on temperature.

Foreign-broadened continuum coefficients have been inferred from both transmission measurements and downwelling atmospheric radiance measurements. In the rotation band between 630 and 800 cm^{-1}, continuum coefficients were inferred from downwelling radiance measurements made in the Arctic at surface temperatures of −33° to −28 °C by Tobin *et al.*[8]; these agreed with earlier measurements made at +23 °C by Burch *et al.*,[9] indicating no temperature dependence for this spectral region. In the ν_2 band, continuum coefficients have been inferred

P. M. Rowe (prowe@harbornet.com) is with the Department of Chemistry, University of Washington, Seattle, Washington 98195. V. P. Walden is with the Department of Geography, University of Idaho, Moscow, Idaho 83844. S. G. Warren is with the Department of Atmospheric Sciences, University of Washington, Seattle, Washington 98195.

Received 27 September 2005; accepted 6 January 2006; posted 15 February 2006 (Doc. ID 64921).

0003-6935/06/184366-17$15.00/0

from laboratory transmission measurements made at temperatures near +23 °C by Tobin *et al.*[10] and from downwelling radiance measurements[11,12] made at locations where surface temperatures were close to +22 °C. (Although the downwelling radiance can be sensitive to the entire atmosphere, most of what is measured is emitted by the lower troposphere, where most of the water is located.) In addition, continuum coefficients in the ν_2 band were inferred from measurements of horizontal transmission in ambient air at −4 °C by Theriault *et al.*[13]

In this work, we infer foreign-broadened continuum coefficients of water vapor in the ν_2 band from measurements of downwelling radiance and atmospheric transmission at temperatures near −30 °C. Transmission measurements were made along a horizontal path at the surface with the South Pole Transmissometer (SPT) during January and December 2000, as part of the South Pole Atmospheric Radiation and Cloud Lidar Experiment (SPARCLE).[14] Measurements of temperature and humidity were made along the transmission path during the SPT measurements. Atmospheric emission measurements were made with an interferometer described in this paper. Measurements were made in January and December 2003 at Dome C, Antarctica.[15]

The use of the Antarctic Plateau as natural laboratory for low-temperature water vapor had several benefits. Tropospheric temperatures are usually below −25 °C. The transmission measurements at the South Pole benefited from the flat landscape and periods of high near-surface atmospheric stability, which minimized temporal and spatial variability in water vapor and temperature. In addition, concentrations of the radiatively important trace gases were monitored routinely by the Climate Monitoring and Diagnostics Laboratory (CMDL) of the National Oceanic and Atmospheric Administration (NOAA). At Dome C, radiosondes were launched routinely to measure the vertical temperature and humidity structure of the atmosphere. Wind speeds in the atmosphere over Dome C are very low[16]; thus the radiosondes sampled a narrow vertical column of air above Dome C that is similar to the column of air measured by the interferometer. Finally, the Antarctic atmosphere is the most pristine on Earth, so there was little emission or absorption of radiation by pollutants.

The continuum is defined conventionally to be the observed absorption coefficient excluding the peaks of strong lines.[8,17] The sum of all the peaks is termed the local line shape, k_{local}; it is equal to the Lorentz line shape within $\pm 25\ \text{cm}^{-1}$ from the line center minus the Lorentz line shape at $25\ \text{cm}^{-1}$. The continuum is composed of a foreign-broadened continuum C_f and a self-broadened continuum C_s. The absorption coefficient of water vapor k is then expressed as

$$k = C_f\left(\frac{\rho_f}{\rho_o}\right) + C_s\left(\frac{\rho_s}{\rho_o}\right) + k_{\text{local}}, \tag{1}$$

where C_f and C_s are cross sections with units of $\text{cm}^2\ \text{molecule}^{-1}$, and ρ_f and ρ_s are the densities of air and water vapor (molecule cm^{-3}). The quantity ρ_o is a reference broadener density defined as $\rho_o \equiv P_o/k_bT_o$, where $P_o = 1013$ mbars, $T_o = 296$ K, and k_b is Boltzmann's constant. The self-broadened continuum is negligible between 1300 and 2000 cm^{-1} at −30 °C and is not considered here.

The literature often reports $C_f{}^o$ rather than C_f; the two are related by

$$C_f = \nu \tanh[hc\nu/(2k_bT)]C_f{}^o, \tag{2}$$

where ν is the wavenumber in cm^{-1}, h is Planck's constant, c is the speed of light, and T is the temperature.[17] The temperature dependence of $\tanh[hc\nu/(2k_bT)]$ is negligibly small (<0.15 parts per thousand per degree) for the spectral range and temperatures considered here. We report C_f and refer to it as the continuum coefficient.

2. Atmospheric Emission Experiment

Atmospheric emission can be simulated given a profile of atmospheric variables such as pressure, temperature, and trace gas concentrations as well as line-shape parameters and continuum coefficients. Here, the atmospheric profile is based primarily on radiosonde data, and the line-shape parameters are supplied by the HITRAN database. The continuum coefficient is inferred by repeating the forward calculation of atmospheric emission while varying the continuum coefficient until the difference between measured and simulated radiances is minimized. Uncertainties in the continuum, therefore, result from uncertainties in the measured radiances, atmospheric variables, and line-shape parameters. Because the temperature of the atmosphere is not constant, radiative transfer simulations were also used to determine the continuum emission contribution of atmospheric layers. From this weighting, an effective temperature of the continuum was determined.

A. Experimental Setup and Ancillary Measurements

Measurements of atmospheric emission were made with the Polar Atmospheric Emitted Radiance Interferometer (PAERI), an atmospheric emitted radiance interferometer (AERI) modified for our use. The AERI instrument was developed by the Space Science and Engineering Center (SSEC) at the University of Wisconsin. The AERI is a ground-based Fourier-transform infrared (FTIR) spectrometer that passively measures atmospheric emission.[12,18,19] The PAERI differs from a typical AERI in that it can view the atmosphere and surface at any angle from 0 (zenith) to 180 deg (nadir).

The interferometer was manufactured by the ABB Bomem Corporation, Model MR-100. The calibration sources were constructed by the SSEC. The detector is a sandwich indium antimonide/mercury cadmium telluride (InSb/MCT) detector, cooled with a Stirling

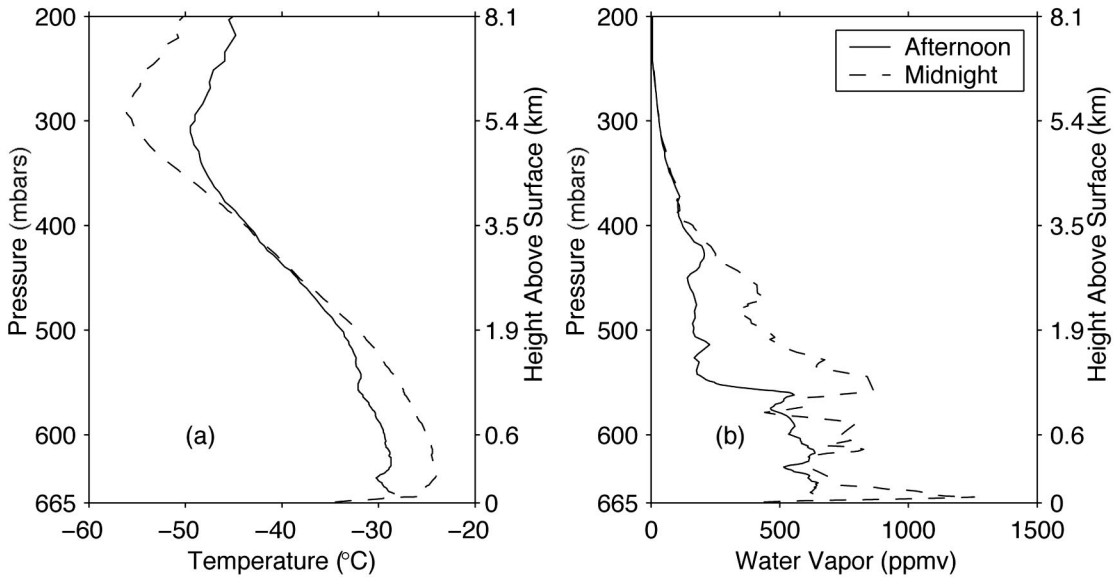

Fig. 1. Temperature and water-vapor profiles for the PAERI measurements of 15 January (afternoon) and 12 December 2003 (midnight) at Dome C. ppmv, parts per million by volume.

cooler to 68 K. It has two channels: channel 1 for frequencies 500–1800 cm^{-1} and channel 2 for 1750–3000 cm^{-1}. The PAERI was housed in an insulated, heated box with a port for viewing the atmosphere. Two calibration sources were used, one warmed to 30–60 K above ambient; the other was warmed just enough to prevent formation of frost within the blackbody cavity.

The PAERI recorded emission spectra nearly continuously during operation at Dome C. Atmospheric conditions during the austral summer field seasons were carefully screened for hydrometeors. Of the clear time periods identified, two were selected that coincided with atmospheric soundings: an afternoon spectrum taken on 15 January 2003 from 15:17 to 16:01 local time (LT) (7:17 to 8:01 UT) and a midnight spectrum taken on 12 December 2003 from 23:51 to 00:38 LT (15:51 to 16:38 UT).

Temperature, pressure, and relative humidity were measured on balloonborne radiosondes at Dome C during the two PAERI measurements. The radiosonde launched in January was a Vaisala RS80-GH sonde while that launched in December was a Vaisala RS90 sonde. For both types of radiosonde, the humidity sensor is a Vaisala HUMICAP, the temperature sensor is a THERMOCAP capacitive bead, and the pressure sensor is a BAROCAP capacitive aneroid.[20]

When an RS80 radiosonde is moved quickly through a temperature gradient of ~50 °C, the thermal shock can cause errors in the sensors.[21] To minimize error due to thermal shock, the radiosondes at Dome C were stored at low temperatures; the storage area was ~20 deg warmer than ambient in January and at ambient temperature in December. Furthermore, the radiosondes were allowed to equilibrate at the surface for at least 10 min before launch.[15] Finally, temperature, pressure, and humidity were measured at the ground at ambient temperature for the last 5 min before the launch to ensure that they were stable prior to the launch.

At very low temperatures, the pressure, temperature, and humidity sensors on the RS80 radiosonde experience lags.[21,22] Several methods of correcting the lags were attempted, but comparison of measured to simulated radiances suggested that errors remained that were larger than the corrections. Instead, we adjusted the temperature and water-vapor profiles using the measured and simulated radiances. The temperature profile was corrected by means of constrained linear inversion,[23] using radiances within the CO_2 band (650–760 cm^{-1}). Temperature corrections were determined in four atmospheric layers: 0–10, 10–200, 200–1500, and 1500–4000 m. The temperature correction for each iteration was constrained to be small to minimize model errors. The new temperature profile was then calculated and the inversion was performed again to give subsequently smaller temperature corrections, to converge on the corrected temperature profile. The temperature correction method is described by Rowe.[24] Temperatures in the afternoon profile were reduced by 0.5–1 K. The temperatures at the surface and at 40 m in the midnight profile were modified by +1 and −3 K. To improve the humidity profiles, the water-vapor amounts were scaled by a common factor at all heights to decrease the residuals at the centers of strong water-vapor lines. The water-vapor amount in the afternoon profile was increased by 10% and in the midnight profile by ~20%.

Figure 1 shows the temperature and water-vapor profiles in the lowest 8.1 km. In January, the PAERI's height was 6 m, and in December it was only 40 cm above the surface. The pressures and temperatures of the atmosphere above the top of the soundings were

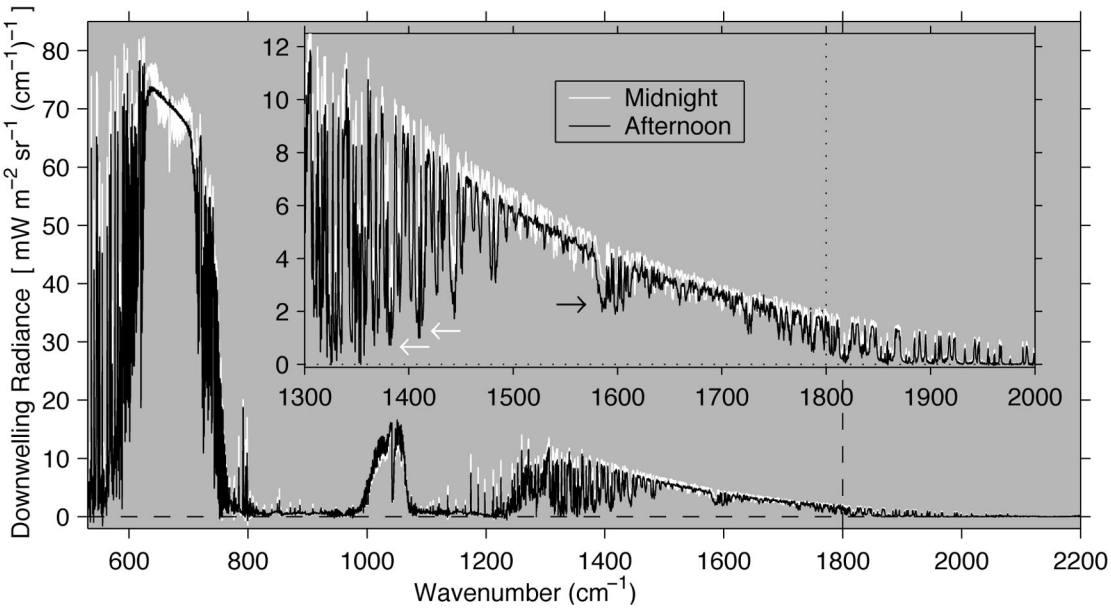

Fig. 2. Calibrated downwelling radiance spectra measured by the PAERI on 15 January 2003 (afternoon) and 12 December 2003 (midnight). Both spectra were measured at Dome C in the vertical (zenith) direction. The radiance from 400 to 1800 cm^{-1} was measured using the channel 1 detector and the radiance from 1750 to 2200 cm^{-1} was measured using the channel 2 detector. The inset shows an expanded view of the water-vapor ν_2 band. The arrows indicate microwindows, as described in the text.

taken from the model atmosphere of a typical January at the South Pole.[25] The water-vapor amount at heights more than 6.6 km above the surface (pressures less than 250 mbars) was set to ~6 parts per million (ppm) based on the estimate made by Walden *et al.*[25] The concentrations of CO_2, N_2O, CH_4, and CFCs were based on the monthly mean values measured at South Pole Station at the surface by NOAA CMDL. The mixing ratios of these gases were assumed to remain constant with height. The atmospheric profile of ozone was based on ozone soundings at South Pole Station. The ozone profile was scaled to minimize the downwelling radiance residual in the 9.6 μm ozone band. Trace gas concentrations in the upper atmosphere were assumed to decrease according to Walden *et al.*[25] For the concentrations of O_2, NO, SO_2, NO_2, NH_3, HNO_3, OH, HF, HCl, and HBr, the subarctic winter standard model of McClatchey *et al.*[26] was used.

B. Emission Measurements

The afternoon and midnight emission measurements are shown in Fig. 2. These were taken in the zenith direction. (The analysis also includes a second afternoon spectrum taken at 7.7 deg from zenith; it is nearly identical to that at zenith.) Each spectrum is actually an average of several spectra measured during one of the two chosen experimental time periods. Parameters for the averaged emission spectra are given in Table 1. A radiance unit is defined here to be 1 mW m^{-2} sr^{-1} (cm^{-1})$^{-1}$. The vertical dashed line in Fig. 2 separates the two detector channels, although the channels overlap between 1750 and 1800 cm^{-1}. The inset shows an expanded view of the ν_2 band with radiance values that generally decrease toward higher frequency (larger wavenumber).

The general shape observed in the emission spectrum is due to the variation of the Planck function with wavenumber, but the detailed structure is more complicated. The Planck function gives the maximum emission possible at a given wavenumber. The emission can reach this maximum at frequencies where the absorption coefficient is very large; these frequencies are termed saturated. The spectral regions between ~1480 and 1580 cm^{-1} and between 1620 and 1700 cm^{-1} are approximately saturated. The Planck function also depends on temperature, so the magnitude of these radiances is determined by the temperature structure near the PAERI instrument. The radiance values in the midnight spectrum vary because of the strong near-surface temperature inversion present at night (Fig. 1). The radiance val-

Table 1. Summary of Parameters for Emission Spectra

Quantity	15 January 2003	12 December 2003
Time period	7:17–8:01 UT 15:17–16:17 LT	15:51–16:38 UT 23:51–00:38 LT
Atmospheric sounding	7:33–9:03 UT	15:30–16:44 UT
Spectra averaged, N_a	5	7
Coadds per spectrum, N_c	46	90
Zenith angles	0, 7.7 deg	0 deg
Angle of Sun (off horizon)	29.5 deg	8.5 deg
Channel 1 detector, ELW[a]	15,799.23 cm^{-1}	15,798.97 cm^{-1}
Channel 2 detector, ELW	15,799.15 cm^{-1}	15,799.22 cm^{-1}

[a]ELW, effective laser wavenumber.

ues in the afternoon spectrum vary much less with frequency because the lower atmosphere was much more isothermal. Because the emission at saturated frequencies is insensitive to the continuum coefficient, saturated frequencies are not useful for inferring continuum coefficients. Instead, unsaturated frequencies are used.

Most of the frequencies in the spectral regions 1300–1480 cm^{-1}, 1580–1620 cm^{-1}, and 1800–2000 cm^{-1} are unsaturated. Such spectral regions with low radiances are called microwindows because they are located between strong lines. Much of the emission in a microwindow, therefore, comes from the continuum, making these ideal spectral regions from which to retrieve the continuum coefficient. A few microwindows in both spectra are indicated by white arrows in Fig. 2, while the black arrow indicates microwindows in the afternoon but not the midnight spectrum.

C. Simulated Radiances

A simulated afternoon spectrum of downwelling radiance and a simulated midnight spectrum were created using the afternoon and midnight sonde profiles as input. To give accurate downwelling radiances, fine vertical spacing in the profile levels is needed near the surface; coarser spacing is acceptable higher in the atmosphere. The desired accuracy for our application requires that the atmospheric profile extend to 60 km.[25]

Radiances were simulated using version 7.1 of the line-by-line radiative transfer model (LBLRTM).[27] The LBLRTM imports line parameters from the HITRAN database[28–30] and uses them to calculate the local (i.e., noncontinuum) line shape for each gas and layer. The HITRAN 2000 edition, with 2001 updates,[31] was used in this work. LBLRTM version 7.1 uses an update to the CKD continuum model by Mlawer and Tobin (MT), the MT-CKD version 1.0 continuum[32] and allows the foreign-broadened continuum of water vapor to be set to zero or multiplied by a factor. The spectral resolution of the simulated spectra was matched to that of the PAERI spectra (0.48 cm^{-1}).

D. Inferring the Continuum Coefficients

To infer continuum coefficients from downwelling radiance spectra, the most direct method is to simulate the downwelling radiance while varying the continuum coefficients until the residual radiance between the simulated and the measured spectra is minimized. This method can make use of an input parameter of the LBLRTM that multiplies the foreign-broadened continuum of water vapor. Since the multiplier is constant with wavenumber, the radiance residual must be minimized at each wavenumber. Turner *et al.*[12] derived multipliers that matched their downwelling radiance to LBLRTM simulations using the CKD version 2.4 continuum[17]; their results were used to specify the MT-CKD continuum.

The method used here is essentially equivalent to that used by Turner *et al.* except that the calculation of atmospheric emission was performed independently of the LBLRTM. The optical depth for each atmospheric layer was simulated using the LBLRTM, but without continuum emission. The optical depth of the continuum in each layer was calculated separately, using a frequency-dependent continuum multiplier. From the combined optical depths of each layer, the downwelling radiance was then calculated. Separating the optical depth in this manner allowed frequency-dependent continuum multipliers to be determined without additional LBLRTM runs. More importantly, a temperature-dependent continuum coefficient could be tested.

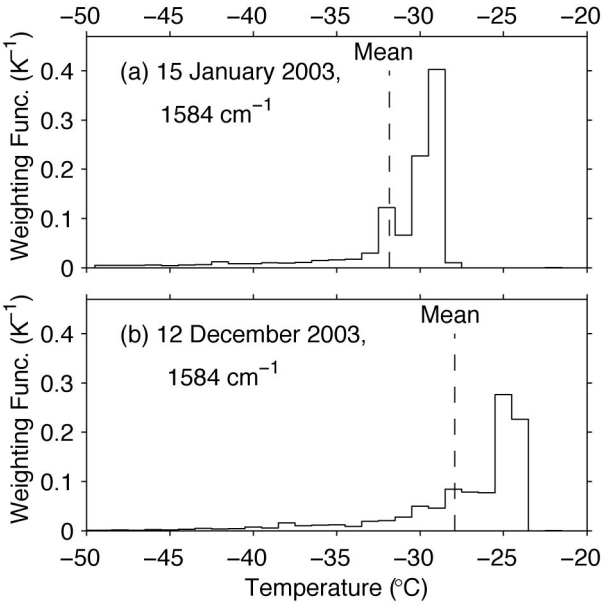

Fig. 3. Continuum weighting function for PAERI data sets of 15 January 2003 and 12 December 2003 for 1 deg bins. The continuum weighting functions at other wavenumbers used to infer continuum coefficients look similar.

E. Effective Temperature

Since the atmosphere emits infrared radiation over a range of temperatures, it is important to determine an effective temperature at which the water-vapor continuum emits. To determine the range of temperatures important for continuum emission, each atmospheric temperature was weighted by its importance to the continuum as seen by an instrument at the surface. The weighting function for temperature T_i is the (normalized) absolute difference between two simulated downwelling radiances; one including the MT-CKD continuum in all layers and the other including it in all layers except those with temperature T_i, in which the continuum is set to zero. Figure 3 shows the weighting functions at 1584 cm^{-1} for the two data sets. The weighted mean temperatures are approximately −32° and −28 °C, indicated by the vertical dashed lines. For each data set, the weighting functions are similar at all the wavenumbers used to infer continuum coefficients, and the mean

temperatures derived for each wavenumber vary by less than 1 K from the value at 1584 cm^{-1}.

F. Averaging Continuum Coefficients

Because the continuum is assumed to vary slowly with frequency, the continuum coefficients at nearby wavenumbers can be averaged to reduce sources of error that are uncorrelated with wavenumber. However, some sources of error are strongly correlated with wavenumber. In particular, measurements closer to a strong line are less reliable for the purpose of retrieving a continuum coefficient than those in a transparent microwindow; thus only the measurements in the microwindows should be averaged. Therefore, the challenge is to pick the continuum coefficients that, when averaged, result in the lowest possible uncertainty. To do this, an algorithm for determining the combined uncertainty was devised that handles correlated and uncorrelated uncertainties differently; the uncorrelated uncertainties are reduced by averaging, but the correlated uncertainties are not.

Continuum coefficients were considered in bins spanning ~10 wavenumbers (or ~20 measurements). First, measurements with uncertainty estimates greater than three times that of a neighbor within 5 cm^{-1} were eliminated (such points were close to strong line centers). For the remaining points in the bin, the uncertainty associated with each possible combination of points was determined according to Eqs. (3)–(6). The combination with the lowest uncertainty was used. In practice, the lowest uncertainties were obtained from combinations of one to eight measurements. Of the final set of averaged continuum coefficients determined in this manner, only those with uncertainties ≤2 continuum units (CU) (1 CU = 10^{-22} cm^2 $molecule^{-1}$) were kept.

The continuum coefficient within each bin is a weighted average of those points deemed worth including and is given by

$$\overline{C_f} = \frac{\sum w_i C_{f,i}}{\sum w_i}. \tag{3}$$

The weights w_i are given as

$$w_i = \frac{1}{\varepsilon_{i,c}{}^2 + \varepsilon_{i,r}{}^2}, \tag{4}$$

where $\varepsilon_{i,c}$ is the error in C_f at wavenumber i due to sources of error that are correlated with wavenumber and $\varepsilon_{i,r}$ is the error that is random with wavenumber, so that $\varepsilon_{i,r}{}^2$ is a variance. We define

$$\varepsilon_c{}^2 \equiv \frac{\sum w_i \varepsilon_{i,c}{}^2}{\sum w_i}, \tag{5}$$

$$\varepsilon_r{}^2 = \frac{\sum w_i{}^2 \varepsilon_{i,r}{}^2}{\left(\sum w_i\right)^2}. \tag{6}$$

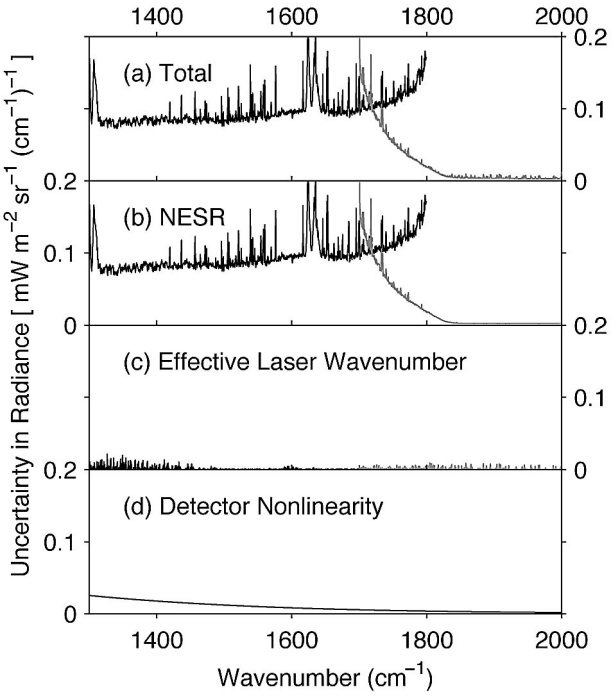

Fig. 4. Uncertainty in the spectrum measured by the PAERI on 15 January 2003 (afternoon): (a) combined uncertainty and (b)–(d) contributing uncertainties. Where the uncertainty differs for the two detectors, the uncertainty for the channel 2 detector is shown as a gray curve.

The expression for ε_r is derived by analogy with Eqs. 4.10 and 4.18 in Bevington and Robinson.[33]

G. Uncertainty Analysis

1. *Uncertainty in Measured Radiance*

Figure 4(a) shows the total uncertainty in the afternoon spectrum measured using the channel 1 detector (black) and channel 2 detector (gray). The spectra were corrected to remove the effects of the finite field of view as described in Ref. 19. Important sources of uncertainty include the noise-equivalent spectral radiance [NESR, Fig. 4(b)], uncertainty in the effective laser wavenumber (ELW) [Fig. 4(c)], and uncertainty in detector nonlinearity correction [Fig. 4(d)]. These are discussed below. Uncertainties for the midnight spectrum were similar, except as noted below. Other sources of uncertainty exist but are negligible compared with these; they are described for a typical AERI by Knuteson *et al.*[19]

Because apodization of the interferometric data reduces the spectral resolution and sensitivity studies show that it produces no benefit to our analysis, the data are not apodized.

Noise occurs in all spectra, including not just the sky spectrum but also the spectra of the hot and ambient calibration sources. Thus the NESR must be determined by propagation of errors, making use of the calibration equation (given by Revercomb *et al.*[34]). The PAERI measures many individual spectra of the sky, S_S, and averages them to give a coadded sky spectrum, $\langle S_S \rangle$. In addition, the PAERI saves the sum

of squares of S_S. Since the number of coadded spectra is known, we can calculate $\langle S_S{}^2\rangle$. The variance of S_S is then given as

$$\sigma_{S_S}{}^2 = \langle S_S{}^2\rangle - \langle S_S\rangle^2. \quad (7)$$

The uncertainty in the coadded spectrum is then $\sigma_{\langle S_S\rangle} = \sigma_{S_S}(2N_c)^{-1/2}$, where N_c is the number of coadded spectra. Since the number of coadded spectra exceeds 45 (Table 1), $\sigma_{\langle S_S\rangle}$ corresponds to a confidence interval of 68%. The factor of 2 accounts for the averaging of measurements from forward and backward interferograms. Equations for the uncertainties in the spectra of the hot and ambient calibration sources are similar but are divided by an additional factor of 2 because a spectrum of each calibration source is measured before and after the measurement of the sky and the two are linearly interpolated as part of the calibration procedure.

The uncertainty in the calibrated, coadded sky spectrum, ΔI, due to noise is then given by

$$(\Delta I)^2 = \left(\frac{\mathrm{d}I}{\mathrm{d}\langle S_S\rangle}\right)^2 \sigma_{\langle S_S\rangle}{}^2 + \left(\frac{\mathrm{d}I}{\mathrm{d}\langle S_H\rangle}\right)^2 \sigma_{\langle S_H\rangle}{}^2 + \left(\frac{\mathrm{d}I}{\mathrm{d}\langle S_A\rangle}\right)^2 \sigma_{\langle S_A\rangle}{}^2, \quad (8)$$

where $\langle S_H\rangle$ and $\langle S_A\rangle$ are coadded spectra of the hot and ambient calibration sources. Each partial derivative is determined by differential error analysis of the emission calibration equation.

Spectra used to infer continuum coefficients were averages of several coadded spectra N_a (see Table 1); thus the NESR for these averages is given by Eq. (8) divided by the square root of N_a. Finally, because we keep only the real part of I (the imaginary part of the spectrum is expected to be only noise[34]), we divide by an additional factor of the square root of two, giving

$$\mathrm{NESR} = \frac{\Delta I}{\sqrt{2N_a}}. \quad (9)$$

An independent estimate of the NESR is given by the imaginary part of the calibrated radiance[19]; it is similar to that given by Eq. (9).

The effective wavenumber of the helium–neon laser in the interferometer was determined using the method described by Knuteson *et al.*[19] The ELWs were different for the afternoon and midnight spectra (Table 1) because the detector was realigned between those dates. Note that while Knuteson *et al.* used a large set of measurements to determine the ELW, this work uses only the spectra from each data set. The standard deviations in ELW values within each data set suggest conservative uncertainty estimates of 1 and 3 ppm (1 standard deviation) for the channel 1 and 2 detectors. A sensitivity study was carried out to determine the uncertainty in the downwelling radiance due to the uncertainty in the ELW [Fig. 4(c)].

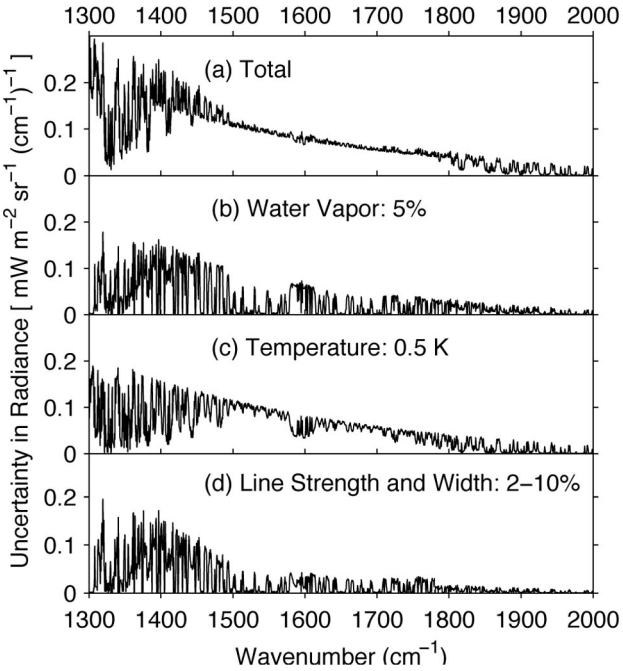

Fig. 5. Uncertainty in simulated radiances for the PAERI measurement of 15 January 2003: (a) combined uncertainty and (b)–(d) most important contributing sources of uncertainty. The magnitudes of the uncertainties in each variable are indicated.

Since the uncertainty in the downwelling radiance was found to change rapidly with frequency from positive to negative values, the uncertainty in the final continuum coefficients can be decreased by averaging continuum coefficients at nearby frequencies.

The nonlinear response of the detector was corrected by the PAERI processing software using the method given by Knuteson *et al.*[19] Uncertainty in the correction is expected to be less than 0.2% of the radiance from the ambient calibration source [Fig. 4(d)].

2. *Uncertainty in Simulated Radiance*

Uncertainties in the simulated downwelling radiances were calculated numerically by perturbing the LBLRTM input values of temperature, pressure, and trace gas amounts (derived from the radiosondes) to determine the sensitivity of the computed downwelling radiance to each atmospheric variable. Figure 5(a) shows the total uncertainty in the simulated radiance based on the afternoon profile, and Figs. 5(b)–(d) show the radiance uncertainties due to uncertainty in the water-vapor amount, temperature, and the line strengths and widths. To calculate the uncertainty due to uncertainties in the line strengths and widths in the HITRAN database, these parameters were perturbed by the uncertainty at the low end of the range given in the database, corresponding to frequency-dependent uncertainties of 10–20%. However, this resulted in errors in downwelling radiance that were considerably larger than the observed difference between measurement and simulation. Furthermore, Rothman[35] suggested that the range given in the HITRAN database may be too large. The un-

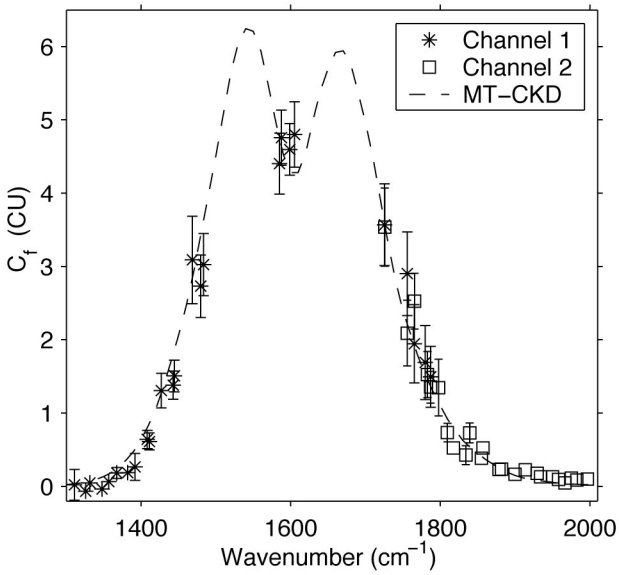

Fig. 6. Continuum coefficients inferred from the PAERI measurement from the afternoon on 15 January 2003 (−32 °C) for both detector channels. The CU is 10^{-22} cm^2 $molecule^{-1}$.

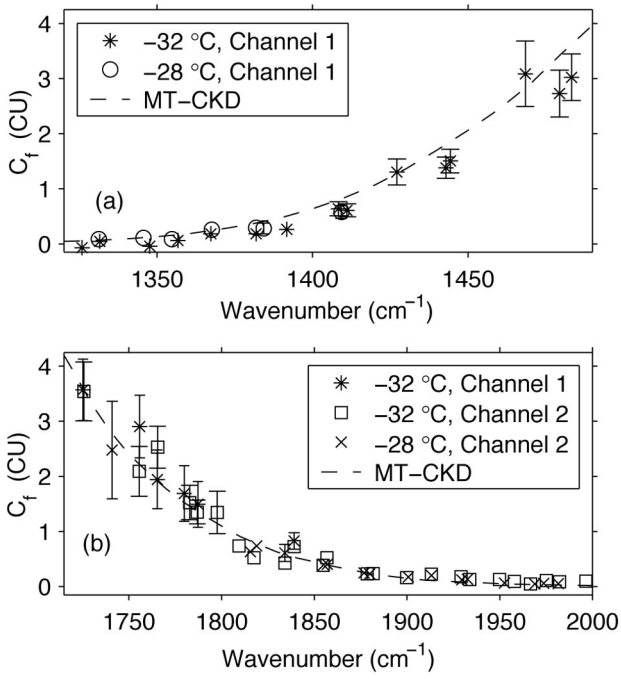

Fig. 7. Continuum coefficients inferred from the PAERI measurements using the afternoon spectrum from 15 January 2003 (−32 °C) and the midnight spectrum from 12 December 2003 (−28 °C) in the (a) low-wavenumber and (b) high-wavenumber wings of the ν_2 band for both detector channels.

certainty at each frequency was thus scaled down by a factor of 5 to give a new uncertainty range of 2–10%, a range considered reasonable by Clough.[36] Uncertainties due to other trace gases are negligible.

H. Results

Figure 6 shows the continuum coefficients inferred from the afternoon spectrum (effective temperature of −32 °C). Also shown is the MT-CKD continuum. At the center of the band, around 1600 cm^{-1}, our derived continuum coefficients are slightly greater than the MT-CKD coefficients. There are results from both detector channels between 1720 and 1790 cm^{-1}; all of the error bars for the channel 1 coefficients overlap with those of nearest-neighbor channel 2 results. Figure 7 shows the two wings of the band in more detail, combining the results from the afternoon and midnight spectra; the midnight spectrum has an effective temperature of −28 °C. In Fig. 7(a), error bars on six of the seven microwindows from the midnight spectrum overlap with their nearest neighbors from the afternoon spectrum. In this spectral region, our continuum coefficients are lower than the MT-CKD continuum coefficients. In Fig. 7(b), all error bars from the 12 December (midnight) results overlap with nearest neighbors from the 15 January (afternoon) results. From 1725 to 1900 cm^{-1}, there is generally good agreement between our results and the MT-CKD continuum; 20 out of 29 of our continuum coefficients have error bars that overlap with the MT-CKD continuum. From 1900 to 2000 cm^{-1} our continuum coefficients are slightly higher.

3. Atmospheric Transmission Experiment

Water-vapor continuum coefficients can be retrieved by comparing measurements and calculations of atmospheric transmission. The continuum coefficients are determined by taking the ratio of the transmission measurements to the calculations. The transmission calculations utilize measurements of temperature, humidity, and other trace gas concentrations made along the horizontal transmission path, as well as the HITRAN lineshape parameters. Uncertainties in these quantities are estimated, as well as how they contribute to the overall uncertainty in the calculated transmission. These uncertainties are combined with those estimated for the measurements to yield the uncertainty in the retrieved continuum coefficients.

A. Experimental Setup and Ancillary Measurements

The SPT (manufactured by the ABB Bomem Corporation) was used to measure atmospheric transmission. It uses the same FTIR as the PAERI but is reconfigured as an active instrument with an infrared source (Fig. 8). Additional elements include a secondary beam splitter (labeled A in Fig. 8), a light trap to prevent stray light from reaching the detector, a telescope, and two retroreflectors. The SPT was housed inside a heated building. The telescope looked out through a hole cut into the wall, as shown. Because the telescope was inside the room, but open to outside air, the telescope tube was insulated to prevent large temperature gradients in the air cavity within the telescope. The interferometer was kept at a constant 40 °C so that optical elements would not be affected by temperature fluctuations. It was purged with dry nitrogen gas to re-

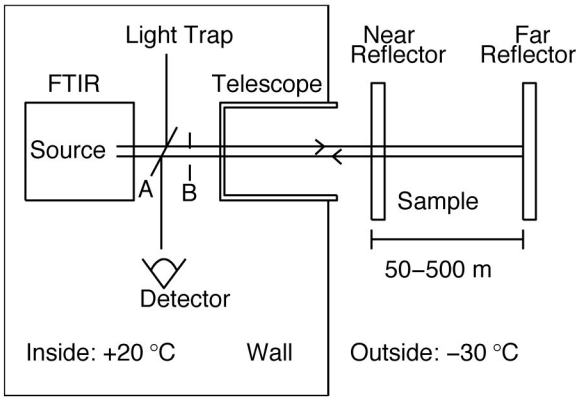

Fig. 8. Schematic of the SPT experiment (not to scale). The wall separates the inside and outside of the building. The optical element at position A is the secondary beam splitter. A flat mirror was placed at position B for tests, but was removed for measurements. The sample is the open atmosphere between the near and far retroreflectors (short and long paths). The near retroreflector is removed when the far retroreflector is in use.

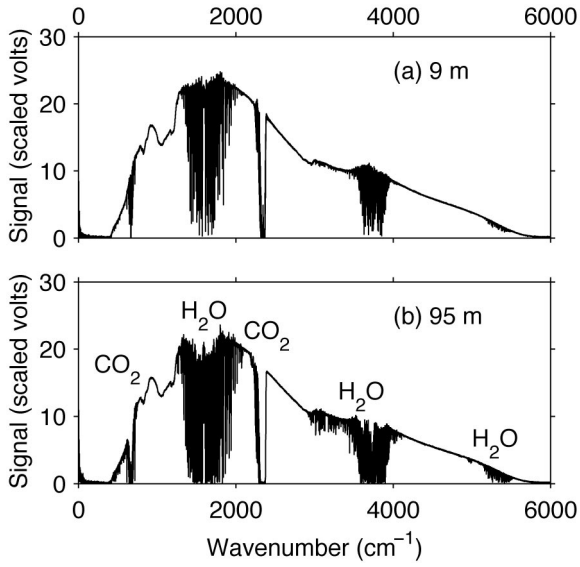

Fig. 9. Example of a (a) short-path signal and (b) long-path signal measured by the SPT in January 2000. Spectral features due to H_2O and CO_2 are labeled in (b).

duce the concentration of water vapor inside the instrument. The detector was an MCT wideband detector (500–5500 cm^{-1}), cooled to 77 K with liquid nitrogen.

As shown in Fig. 8, radiation from the infrared source travels through the interferometer, (and thus the primary beam splitter, not shown in the figure), then through the secondary beam splitter. The telescope nearly collimates the beam, which then travels to either the near or far retroreflector. The near retroreflector is placed a few meters from the telescope, while the far retroreflector is placed from 50 to 500 m away. After striking the retroreflector, the infrared beam is reflected back toward the interferometer, where the radiation travels back through the telescope and is reflected to the detector by the secondary beam splitter. Half of the source radiation is lost in each passage through a beam splitter, so only one quarter of the source radiation is available at the detector after passing through the beam splitter in the interferometer and the secondary beam splitter.

Prior to measurements, the stability of the SPT source was tested. A mirror was placed in the optical path at position B in Fig. 8, just before the telescope. With the mirror in place, the signal at the centerburst of the interferogram was measured as a function of time. The magnitude of the centerburst varied by only 1% over the duration of a measurement sequence.

During a measurement sequence, a short-path spectrum, or background spectrum, is measured with the near retroreflector in place, followed by a long-path spectrum with the near retroreflector removed. The ratio of these measurements yields the transmission between the two retroreflectors. Visual observations during the measurements ensured that the atmosphere was sufficiently free of ice crystals.

Figure 9 shows an example of the short-path (9 m) and long-path (95 m) spectrum measured by the SPT in January 2000. The path lengths are twice the distance from the end of the telescope to the retroreflector. The slowly varying envelope of the source radiation is apparent. Superimposed on this envelope are the broad absorption features of the instrument optics and the fine absorption features of trace gases, mainly CO_2 and H_2O [labeled in Fig. 9(b)]. The spectra are not apodized and have a resolution of 0.48 cm^{-1}.

The transmission path was located along the border of the Clean Air Sector at South Pole Station, ~500 m upwind of the station, so the atmosphere along the transmission path was free of pollution from the station. Air temperature (T_a) and frost-point temperature (T_f) were measured along the transmission path during SPT measurements. Pressure, humidity, and trace gas amounts are measured routinely by NOAA CMDL[37] in the Atmospheric Research Observatory (ARO). The ARO is located ~100 m from our transmission path, also along the border of the Clean Air Sector. The transmission path was surveyed and the relative elevation was found to vary by only 0.4 m in the first 40 m and by 0.2 m within the next 40–500 m. Because the surface was so flat, T_a and T_f varied little along the path; this was confirmed by measurements at two places along the transmission path. Table 2 summarizes the conditions for the measurements.

Our measurements of T_a and T_f were compared with concurrent measurements made by NOAA CMDL near the ARO. For December 2000 and January 2001, the rms difference for T_a was 0.7 K and for T_f it was 0.5 K.

During the SPT measurement used to infer continuum coefficients (5 January 2000), T_a and T_f varied little over the duration of each measurement and even over the 30 min duration of the entire measure-

Table 2. Summary of Parameters for Transmission Measurement (5 January 2000)

Quantity	Value	Uncertainty
Temperature	−29.0 °C	0.2 °C
Frost-point temperature	−32.01 °C	0.05 °C
Pressure	673.5 mbars	0.5 mbars
Two-way long path length	200.0 m	0.5 m
Two-way short path length	2.9 m	0.1 m
$(1 - b_S)/(1 - b_L)$[a]	0.86	—
N_2O	0.32 ppm	5%
CH_4	1.7 ppm	5%
CO_2	366.5 ppm	5%
CO	0.037 ppm	—
CCl_3F	2.64×10^{-4} ppm	—
CCl_2F_2	5.30×10^{-4} ppm	—
CCl_4	1.1×10^{-4} ppm	—

[a]The terms b_S and b_L are the beam divergences for the short and long paths.

ment sequence (Table 2). However, in the analysis below we use more conservative estimates of 1% for water-vapor concentration and 0.25 K for temperature.

The CH_4 and CO_2 concentrations in Table 2 were interpolated from measurements made by the NOAA CMDL Carbon Cycle Greenhouse Gases group at South Pole Station on 31 December 1999 and 10 January 2000.[38–40] The N_2O concentration was measured by NOAA CMDL[37] on 4 January 2000. The concentrations of CCl_3F and CCl_2F_2 were from measurements made by NOAA CMDL using an *in situ* gas chromatograph; for CCl_3F the February 2000 monthly mean was used (no value was given for January) and for CCl_2F_2 the monthly mean for January 2000 was used.[37] The concentration of CCl_4 was based on the monthly mean of measurements by NOAA CMDL in 1992 given by Walden *et al.*[25] For the concentrations of other trace gases the subarctic winter model of McClatchey *et al.*[26] was used. The CO concentration was modified to match simulated and measured transmittances near 2143 cm^{-1}. Conservative uncertainties of 5% were assumed for N_2O, CH_4, and CO_2. Uncertainties in the concentrations of other trace gases are expected to have negligible effects on retrieved continuum coefficients.

B. Inferring Continuum Coefficients

The ratio of the long-path signal S_L to the short-path signal S_S is given as

$$\frac{S_L(\nu)}{S_S(\nu)} = \frac{\int (1 - b_L) S_0(\tilde{\nu}) t_L(\tilde{\nu}) e^{i\phi(\tilde{\nu})} L(\nu,\ \tilde{\nu}) \mathrm{d}\tilde{\nu}}{\int (1 - b_S) S_0(\tilde{\nu}) t_S(\tilde{\nu}) e^{i\phi(\tilde{\nu})} L(\nu,\ \tilde{\nu}) \mathrm{d}\tilde{\nu}}, \tag{10}$$

where ν is the wavenumber, b_L and b_S are the fractions of light lost along each path due to divergence of the infrared beam (due to imperfect collimation), t_L and t_S are the transmittances of the atmosphere over the long and short paths, and ϕ is the phase response of the instrument. S_0 is the source radiation adjusted for the effects of the instrument optics and any gaseous absorption within the instrument. The convolution with the instrument line shape L accounts for the finite resolution. The instrument line shape is assumed to be a sinc function, as for the PAERI instrument, with a width corresponding to the resolution of 0.48 cm^{-1}. In Eq. (10) the limits of integration are from $-\infty$ to $+\infty$, but L is close to zero after several linewidths.

To be taken out of the integral, a given quantity must be approximately constant in wavenumber over the width of L. S_0 is expected to vary slowly with wavenumber because absorption features were minimized by purging with dry nitrogen gas (99.998% pure). To confirm this, a flat mirror was placed at location B in Fig. 8, and the spectrum was recorded. Inspection of the spectrum showed that S_0 varies slowly with wavenumber except near the centers of strong water-vapor lines; the strongest of these would correspond to a transmittance of 0.95. Wavenumbers near the centers of strong lines are not used to retrieve continuum coefficients, so the assumption that S_0 is approximately constant over the width of L should be a negligible source of error.

The beam divergences b_L and b_S are expected to be constant with respect to wavenumber, while the phase is expected to vary slowly with wavenumber. These quantities are also taken out of the integral, giving

$$\frac{S_L(\nu)}{S_S(\nu)} \approx \frac{(1 - b_L) \int t_L(\tilde{\nu}) L(\nu,\ \tilde{\nu}) \mathrm{d}\tilde{\nu}}{(1 - b_S) \int t_S(\tilde{\nu}) L(\nu,\ \tilde{\nu}) \mathrm{d}\tilde{\nu}}. \tag{11}$$

Figure 10 shows the ratio S_L/S_S for various path differences (long minus short). In the absence of beam divergence, the ratio would be unity at transparent wavenumbers, i.e., those for which $t_L \cong t_S \cong 1$. Broadly speaking, transparent wavenumbers are within the ranges of 800–1200 cm^{-1}, 2100–2150 cm^{-1}, and 4100–4800 cm^{-1}. Because of beam divergence, the ratio is less than unity at these wavenumbers. If beam divergence is independent of wavenumber, the ratio will be a constant at transparent wavenumbers [as in Figs. 10(a) and 10(b)]. However, for path lengths greater than 250 m [Figs. 10(c)–10(e)], the ratio is not constant with wavenumber. Therefore these path lengths are not used here to determine continuum coefficients. The ratio $(1 - b_S)/(1 - b_L)$ is determined for path lengths less than 250 m by averaging S_L/S_S over the transparent wavenumbers. For example, $(1 - b_S)/(1 - b_L)$

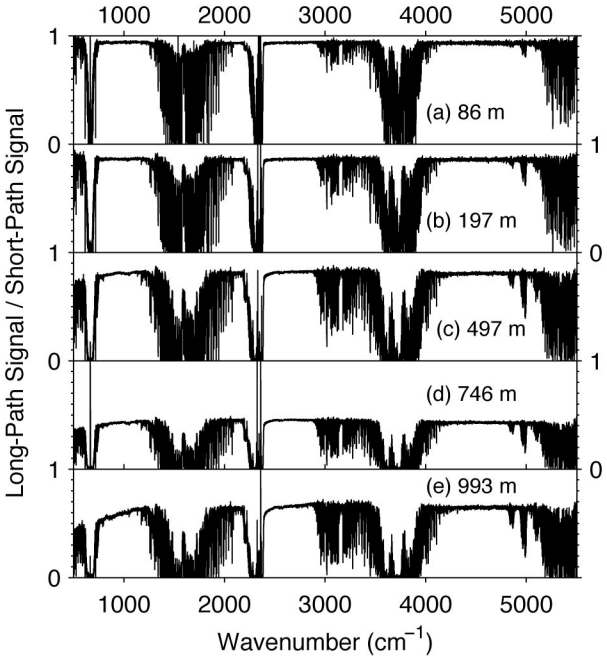

Fig. 10. Magnitudes of the ratios of long-path to short-path signals. The optical path traveled by the light between the two retroreflectors (two way) is indicated in each panel. The return signals generally decrease with path length because of divergence of the beam. For shorter optical paths [(a) and (b)], the ratio is approximately constant in the nearly transparent regions where absorption features are weak (800–1100 cm^{-1}, 2200 cm^{-1}, etc.), but for longer optical paths [(c)–(e)] the ratio increases with wavenumber from 500 cm^{-1} to ~1200 cm^{-1}.

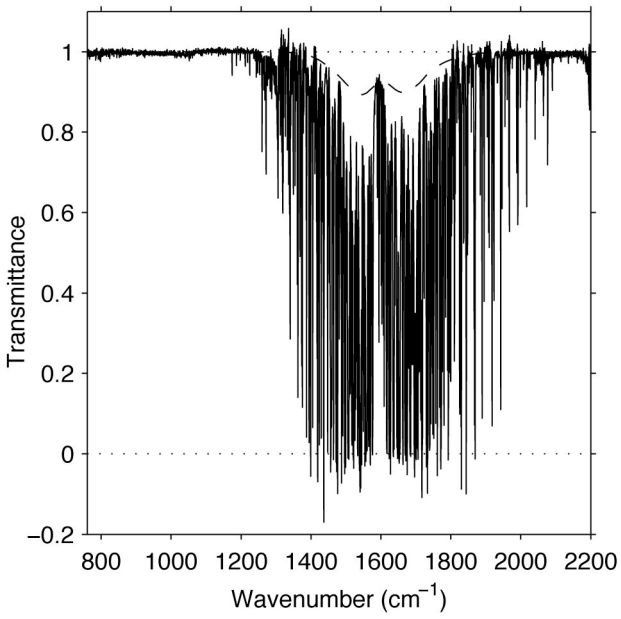

Fig. 11. Transmittance measured by the SPT at the South Pole on 5 January 2000 for an optical path difference of 197 m at −29 °C (black curve). Measured transmittances below zero and greater than one are nonphysical but occur because of the finite spectral resolution. The dashed curve shows the transmittance of the MT-CKD continuum through this path length, simulated with the LBLRTM. The horizontal dotted lines signify transmittances of zero and unity.

= 0.86 in Fig. 10(b). Deviations from this value are categorized as systematic or random, in a manner similar to the sources of uncertainty for the PAERI instrument described above.

We rearrange approximation (11) to give

$$\frac{(1-b_S)}{(1-b_S)}\frac{S_L(\nu)}{S_S(\nu)} \approx \frac{\int t_L(\tilde{\nu})L(\nu,\ \tilde{\nu})\mathrm{d}\tilde{\nu}}{\int t_S(\tilde{\nu})L(\nu,\ \tilde{\nu})\mathrm{d}\tilde{\nu}}. \qquad (12)$$

We define the left-hand side as the measured transmittance. Figure 11 shows the measured transmittance used to infer continuum coefficients from 765 to 2200 cm^{-1}. Absorption by the continuum in the ν_2 band is evident in the spectrum. To make this clear, the transmission of the MT-CKD continuum is shown (dashed curve). Measured transmittances that are greater than the continuum transmittance, greater than one, or less than zero are not physical, but occur because of the effects of finite spectral resolution. These effects are accounted for in the continuum retrieval.

We now define t^c to be the deviation from the expected transmittance and t' to be the transmittance due to the local line shape, the self-broadened continuum of water vapor, the transmittances of all other gases, and the MT-CKD continuum. We will interpret t^c to indicate a temperature dependence of the foreign-broadened continuum. Since the continuum is assumed to vary slowly over the instrument line shape, approximation (12) is equivalent to

$$\frac{(1-b_S)}{(1-b_L)}\frac{S_L(\nu)}{S_S(\nu)} \approx \frac{t_L{}^c(\nu)}{t_S{}^c(\nu)}\left[\frac{\int t_L{}'(\tilde{\nu})L(\nu,\ \tilde{\nu})\mathrm{d}\tilde{\nu}}{\int t_S{}'(\tilde{\nu})L(\nu,\ \tilde{\nu})\mathrm{d}\tilde{\nu}}\right]. \qquad (13)$$

The term in brackets on the right is calculated using the atmospheric variables as input into the LBLRTM.

To infer continuum coefficients, we relate the ratio of correction transmittances (t^c) to a correction to the continuum coefficient by noting that

$$\frac{t_L{}^c(\nu)}{t_S{}^c(\nu)} = \exp\left[-\Delta C_f(\nu)\left(\frac{\rho_f}{\rho_o}\right)\rho_s\Delta Z\right], \qquad (14)$$

where ΔC_f is the correction to the continuum and ΔZ is the difference between the long and short (two-way) path lengths. Putting Eq. (14) into approximation (13) and solving for ΔC_f gives

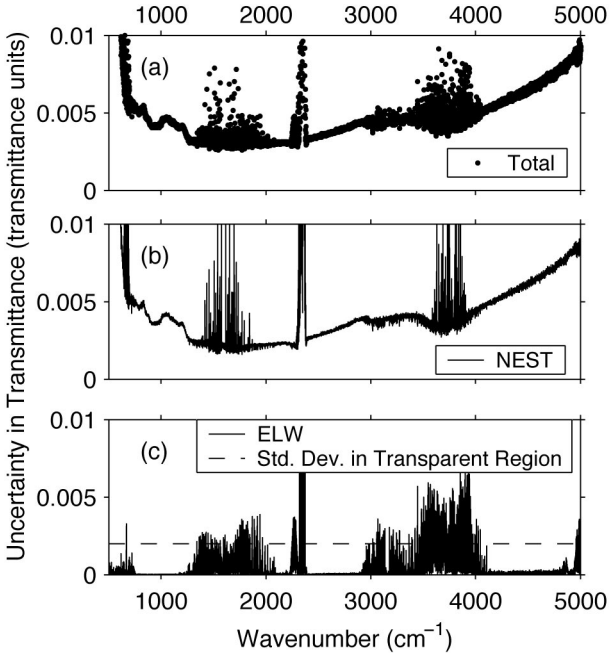

Fig. 12. Uncertainties in the transmittances measured by the SPT on 5 January 2000, caused by instrumental sources of error. The sources of uncertainty, labeled on the figure, are described in the text.

$$\Delta C_f(\nu) \approx \frac{-\rho_o}{\rho_f \rho \Delta Z} \times \ln\left\{ \frac{(1-b_S)}{(1-b_L)} \frac{S_L(\nu)}{S_S(\nu)} \left[\frac{\int t_S'(\tilde{\nu}) L(\nu,\ \tilde{\nu}) \mathrm{d}\tilde{\nu}}{\int t_L'(\tilde{\nu}) L(\nu,\ \tilde{\nu}) \mathrm{d}\tilde{\nu}} \right] \right\}. \quad (15)$$

The values of ρ_f, ρ, and ΔZ were determined from the measurements characterizing the atmospheric path. The instrument line shape L was calculated as described above. The continuum coefficient is then given as $C_f = C^o + \Delta C_f$, where C^o is the MT-CKD continuum.

C. Error Analysis

Because the continuum coefficient is derived from both calculated and measured transmittances, it is important to quantify sources of error in both the measurements and calculations. Figure 12(a) shows the total uncertainty in the measured transmittance. The sources of error contributing to the total uncertainty are from instrument noise, uncertainty in the ELW, and uncertainty in the scaling factor $(1 - b_S)/(1 - b_L)$.

Before discussing sources of error contributing to the total uncertainty, some potential sources of error that were not included in computing the total uncertainty in the measured transmittance are worth mentioning. A nonlinear response of the detector as a function of signal strength can occur in the SPT, as in the PAERI. A review of detector nonlinearity is given by Griffiths and deHaseth.[41] Evidence for detector nonlinearity is an elevation from zero of the signal in the out-of-band region below 700 cm^{-1}.[42] Such evidence is absent from the measured transmittance. The phases of the complex spectra differ slightly for different path lengths, but examination of the difference between the absolute magnitude of the transmittance and the real part of the transmittance showed that this source of error is negligible in the ν_2 band compared with other sources. Stray light can also be a source of error, according to Griffiths and deHaseth.[41] In passing through the secondary beam splitter, half of the modulated source light is reflected at a 90 deg angle rather than being transmitted out along the path. In the SPT, this light is redirected to a light trap to prevent stray light from reaching the detector. Error due to stray light is therefore expected to be minimal.

The noise-equivalent spectral transmittance (NEST) is determined in a manner analogous to the NESR for the PAERI, using differential error analysis. Like the PAERI, the SPT saves a coadded spectrum as well as a sum-of-squares spectrum. From these, the variance for a single spectrum measured by the SPT can be determined. To obtain the variance of the coadded spectrum, the variance for a single spectrum is divided by $2N$, where N is the number of coadds (256) and the factor of 2 accounts for the reduction made by keeping only the real part of the complex transmittance.

To check this method, the NEST was compared with the standard deviation in the transmittance over a spectral region where the transmittance is close to 1.0 (926–944 cm^{-1}). The standard deviation and the NEST were both 3×10^{-3}.

Figure 12(b) shows the NEST. The NEST is small where the signal is largest, and in the ν_2 band the signal is largest at frequencies that are weakly absorbing, in microwindows between strong spectral lines. Because noise is random with frequency, it can be reduced by averaging continuum coefficients at nearby frequencies.

Careful examination of Fig. 11 reveals that the measured transmittance deviates from unity in the nearly transparent regions, where the continuum is negligible. Some deviation is attributable to noise and absorption by trace gases. However, the measured transmittance is slightly lower than the simulated transmittance for 800–1000 cm^{-1} and 2100–2150 cm^{-1}, and is slightly higher for 1000–1200 cm^{-1}. The standard deviation between the measured transmittance and a simulation in these regions was determined to be 0.002 transmittance units. We assume that errors of the same magnitude exist within the ν_2 band [horizontal dashed line in Fig. 12(c)].

The ELW was determined as follows. A simulated transmission spectrum was created with an initial guess for the ELW. The measured and simulated transmittance spectra were interpolated onto a finer

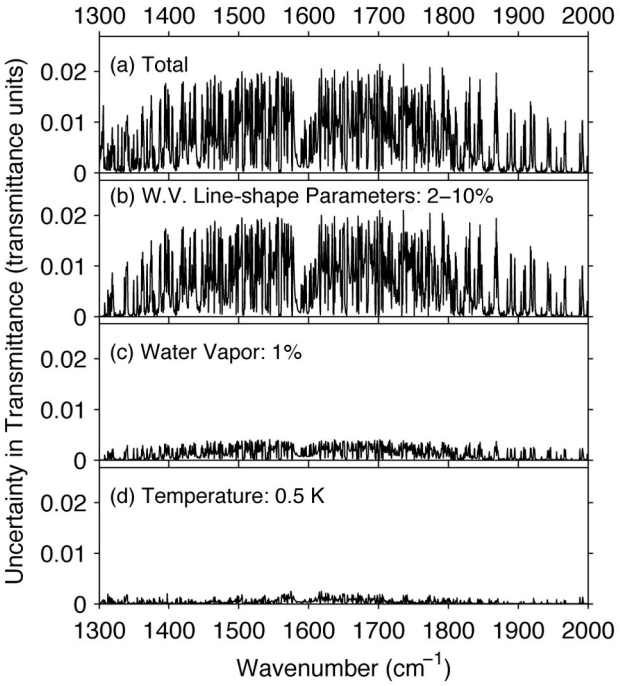

Fig. 13. Uncertainty in the simulated transmittance: (a) the combined uncertainty and (b)–(d) the most important contributing sources of error. The magnitudes of the uncertainties in each variable are indicated. W.V., water vapor.

spectral grid. The wavenumber scale of the measured transmittance was multiplied by a factor to stretch or compress the measured transmittance relative to the simulated transmittance. The optimal factor was found by minimizing the rms difference between 730 and 750 cm^{-1}. The initial ELW is then multiplied by the factor to obtain the ELW. The ELW determined from this method was 15,798.75 cm^{-1}. On the basis of the difference in ELW obtained using forward and backward spectra, the uncertainty was determined to be 1.3 ppm.

The uncertainty in the ELW was propagated to an uncertainty in the transmittance [Fig. 12(c)], which is largest near strong lines where the radiance changes rapidly with wavenumber. Because uncertainties in the transmittance due to uncertainty in the ELW fluctuate rapidly between positive and negative, this source of error can be reduced by averaging nearby frequencies.

Figure 13(a) shows the total uncertainty in the transmission simulated by the LBLRTM. Figures 13(b)–13(d) show the uncertainties in transmittance due to the uncertainties in line strengths and widths, water-vapor amount, and temperature. The total uncertainty includes these as well as the contributions from the uncertainties in CH_4 and N_2O amounts, which are not shown because they are much smaller than the other uncertainties. Each uncertainty was calculated from the sensitivity of the transmission to the particular variable. The uncertainties in the transmittance due to uncertainties in the line-shape parameters were handled in a similar way as those

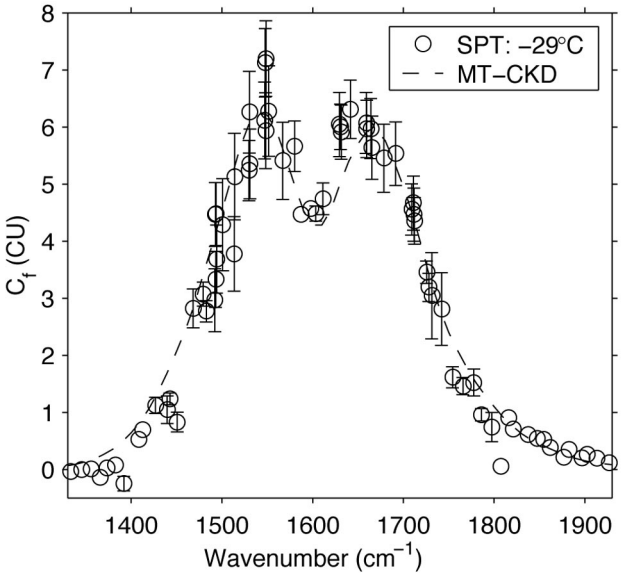

Fig. 14. Continuum coefficient at −29 °C from the 5 January 2000 SPT measurement. Data points have been averaged over bins of ~10 cm^{-1} in the wings and at the center. The MT-CKD continuum coefficient is shown for reference.

for the emission experiment explained above. Figure 13(b) shows that the dominant source of error in the calculated transmittance is uncertainties in line strength and linewidth. This is also the largest source of uncertainty in retrieved continuum coefficients near the two peaks of the band.

D. Results

Figure 14 shows the continuum coefficients inferred from the SPT measurement. The continuum of

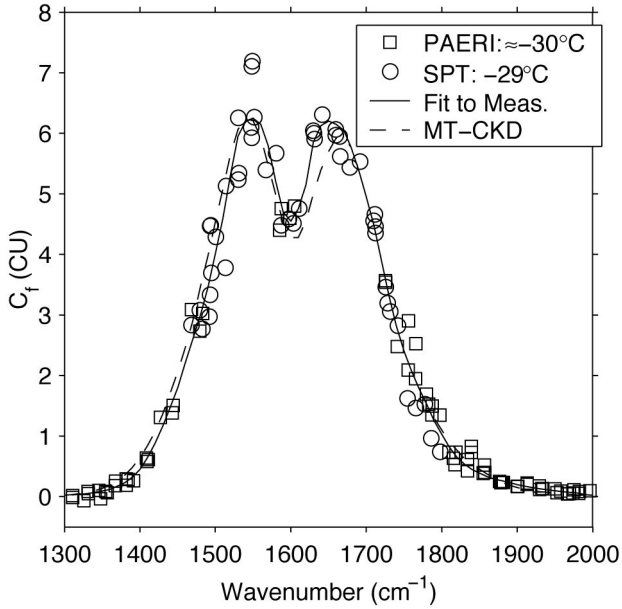

Fig. 15. Foreign-broadened continuum coefficients of water vapor at −30 °C retrieved from the PAERI and SPT measurements. A hand-drawn smooth curve through the data points is shown. Also shown for reference is the MT-CKD continuum.

Table 3. Root-mean-square Deviation between the Measured Results and the Hand-drawn Curve in Fig. 15

Spectral Region (cm^{-1})	rms Deviation (CU)	rms Deviation (%)
1300–1420	0.06	80
1420–1590	0.5	10
1590–1650	0.1	2
1650–1870	0.3	20
1870–1990	0.03	30

MT-CKD version 1.0 is also shown for reference. The error bars on the retrieved continuum coefficients were determined from propagation of errors in simulated and measured transmittances. The same technique described for the PAERI was used to average coefficients over bins of ~10 cm^{-1}. At the center of the band and in the wings, random errors were typically larger than errors that are correlated with frequency, so averaging reduced the combined errors. Near the two peaks of the band (1485–1575 cm^{-1} and 1610–1725 cm^{-1}) there are many strong lines, and the total uncertainty is dominated by uncertainties in the line-shape parameters. Because this source of uncertainty is assumed to be correlated with frequency, it cannot be reduced by averaging. Furthermore, retrieved continuum coefficients varied from 1 to 1.4 times the MT-CKD continuum in this region, and the variation was uncorrelated with errors.

4. Conclusions

Figure 15 shows the foreign-broadened continuum coefficients of water vapor retrieved from the PAERI and SPT measurements together on one plot. Also shown in Fig. 15 is a hand-drawn fit to these results, along with the MT-CKD continuum. Because sources of error for the PAERI are better defined and quantified, only the PAERI results are shown in the wings of the band. (However, note that in Figs. 7 and 14 both PAERI and SPT show similar deviations for the MT-CKD continuum). At 1480 and 1600 cm^{-1} and from 1725 to 1800 cm^{-1}, the PAERI and SPT results agree with each other. The rms deviation of all data points from the hand-drawn fit line is 0.3 CU . The fit is best between 1590 and 1650 cm^{-1}, where the rms deviation is 0.1 CU (2%). The rms deviations over various spectral regions are given in Table 3. Near the peak at 1550 cm^{-1}, points are clustered in two groups at ~6 and 7 CU, making interpretation difficult. The low-temperature continuum is lower than MT-CKD in the low-wavenumber wing and higher near the center of the band.

Table 4 lists the low-temperature continuum coefficients (from the hand-drawn fit line) in 10 cm^{-1} intervals along with the multipliers (relative to the MT-CKD continuum coefficients) that give these coefficients. The multiplier varies from a minimum of 0.64 to a maximum of 2.04.

A. Comparison of Results with Previous Measurements

Figure 16 compares our results with the continuum coefficients of Theriault *et al.*[13] at −4 °C. In the low-wavenumber wing of the ν_2 band [Fig. 16(a)], our results generally agree with those of Theriault *et al.* In the high-wavenumber wing [Fig. 16(b)], the continuum coefficients inferred from the PAERI are con-

Table 4. Foreign-broadened Continuum Coefficients of Water Vapor at −30 °C (243 K) from a Fit to Measurements Made with the PAERI and SPT at Temperatures between −28 and −32 °C, Including the Multipliers of the MT-CKD Continuum

ν (cm^{-1})	C_{243K} (CU)	Multiplier	ν (cm^{-1})	C_{243K} (CU)	Multiplier	ν (cm^{-1})	C_{243K} (CU)	Multiplier
1310	0.03	0.89	1540	6.20	0.99	1770	1.78	1.00
1320	0.04	0.85	1550	6.25	1.01	1780	1.52	1.00
1330	0.05	0.79	1560	6.15	1.04	1790	1.25	0.96
1340	0.07	0.73	1570	5.80	1.06	1800	1.03	0.94
1350	0.09	0.67	1580	5.20	1.04	1810	0.82	0.90
1360	0.12	0.64	1590	4.70	1.04	1820	0.65	0.85
1370	0.17	0.64	1600	4.55	1.06	1830	0.54	0.86
1380	0.23	0.64	1610	4.75	1.11	1840	0.45	0.85
1390	0.32	0.67	1620	5.15	1.13	1850	0.39	0.86
1400	0.45	0.70	1630	5.85	1.17	1860	0.33	0.89
1410	0.64	0.77	1640	6.13	1.14	1870	0.29	0.95
1420	0.88	0.82	1650	6.20	1.09	1880	0.26	1.11
1430	1.16	0.85	1660	6.15	1.04	1890	0.23	1.21
1440	1.47	0.86	1670	6.05	1.02	1900	0.20	1.34
1450	1.80	0.87	1680	5.77	1.00	1910	0.17	1.43
1460	2.20	0.90	1690	5.38	1.00	1920	0.15	1.54
1470	2.60	0.90	1700	4.95	1.00	1930	0.13	1.62
1480	2.98	0.86	1710	4.48	1.00	1940	0.11	1.66
1490	3.45	0.87	1720	3.91	1.00	1950	0.10	1.82
1500	4.00	0.88	1730	3.32	1.00	1960	0.08	1.90
1510	4.60	0.90	1740	2.82	1.00	1970	0.07	1.88
1520	5.30	0.94	1750	2.40	1.00	1980	0.06	2.04
1530	5.95	0.98	1760	2.08	1.00			

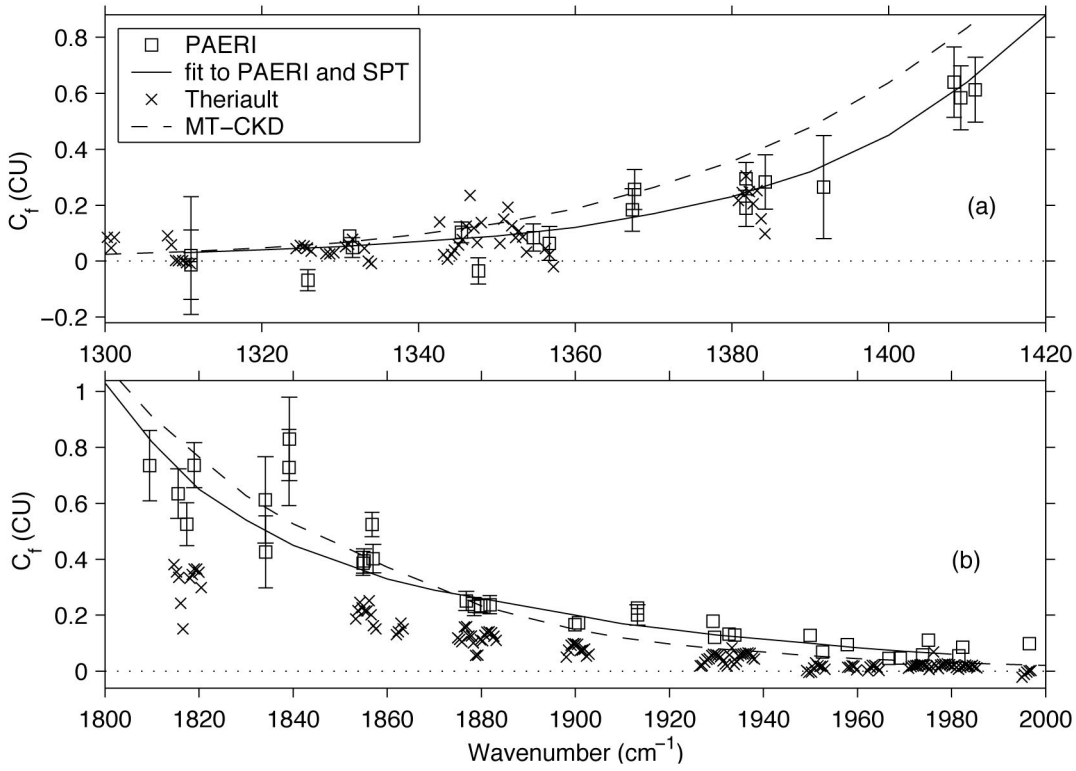

Fig. 16. Comparison of foreign-broadened continuum coefficients retrieved in this work with the results of Theriault *et al.*

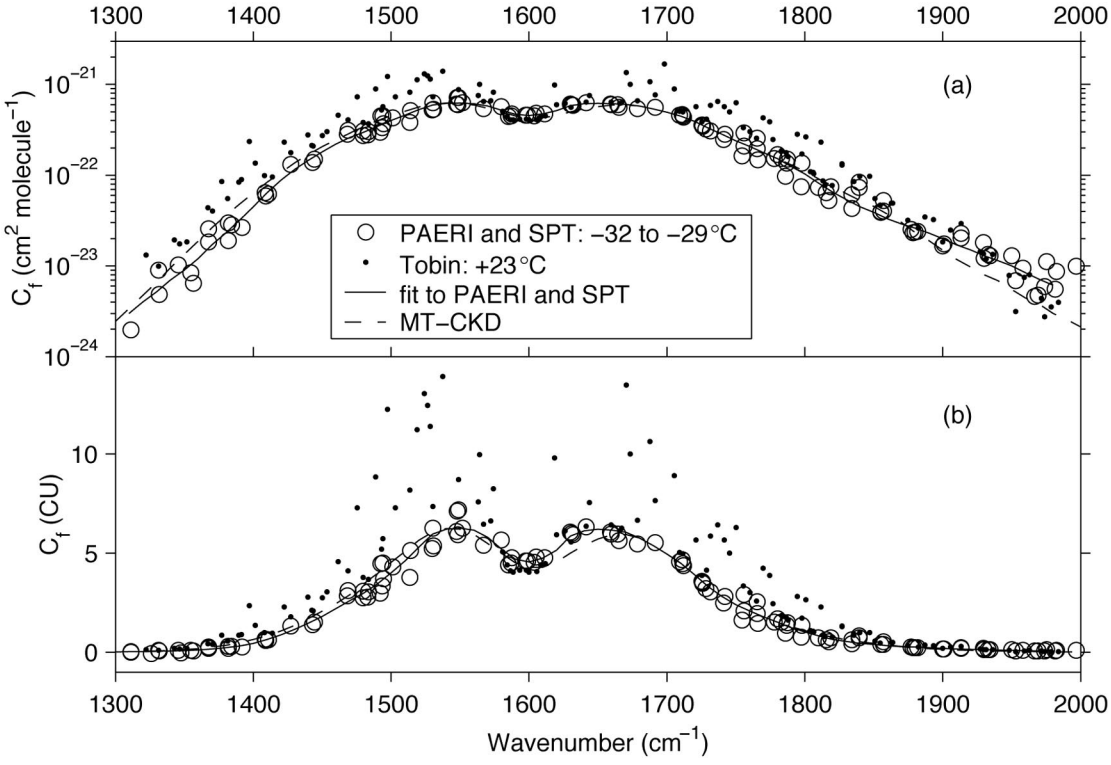

Fig. 17. Comparison of foreign-broadened continuum coefficients retrieved in this work with the results of Tobin *et al.*: (a) on a log scale in units of cm^2 molecule^{-1} and (b) on a linear scale in units of CU.

siderably higher than those of Theriault *et al.* and agree more closely with the MT-CKD continuum.

Figure 17 compares our results with the measurements of Tobin *et al.*[8] at +23 °C on both linear [Fig. 17(a)] and logarithmic [Fig. 17(b)] scales. We can see that Tobin *et al.*'s results were generally higher than these results, indicating a positive temperature dependence, which, from 1300 to 1400 cm^{-1}, agrees with the prediction of Ma and Tipping.[3] However, in two regions the temperature dependence is apparently negative. Near 1600 cm^{-1}, our results are roughly 10% higher than Tobin *et al.*'s, and above 1945 cm^{-1}, our results are roughly 50% higher than Tobin *et al.*'s.

B. Effect on Retrieved Upper-Tropospheric Water Vapor

A sensitivity study was performed to determine the effect of the inferred low-temperature continuum coefficients on upper-tropospheric water-vapor retrievals from a satellite; specifically, by the TIROS (Television and Infrared Observations Satellite) Operational Vertical Sounder (TOVS). TOVS has a channel from 1369 to 1590 cm^{-1} that is sensitive to emission from the atmospheric pressure layer of 200–500 mbars. The corresponding temperature range for a range of terrestrial atmospheres is typically −20 to −60 °C.[26] The mean continuum multiplier over this range is 0.95 and the range is from 0.64 to 1.06.

Using the LBLRTM, the upwelling emission for the channel was calculated for continuum multipliers of 0.7 and 1.0. The calculated upwelling emission for the channel was close to 4.5 radiance units and the brightness temperature was near −37 °C. The relative change in retrieved water-vapor amount ($\Delta H_2O/H_2O$) using a continuum multiplier of 0.7 versus 1.0 was determined to be −0.06, corresponding to a change in brightness temperature of 0.4 K. Since the average of continuum multiplier over the channel was close to 1.0, the new continuum coefficients will have a small effect on retrieved water vapor in this channel. Larger effects would be seen in narrower channels that do not average over positive and negative temperature dependences.

We thank Michael Town and Stephen Hudson for assistance with the SPT measurements. We are grateful to David Tobin for sharing his expertise on continuum coefficients. We thank Eric Salathe of the Joint Institute for the Study of the Atmosphere and Ocean for help with the sensitivity study involving satellite retrievals of upper-tropospheric humidity from TOVS. We acknowledge the Climate Monitoring and Diagnostics Laboratory of NOAA for making their measurements of the concentrations of atmospheric trace gases from South Pole Station available to us. Vital logistical support for our field work at Dome C was provided by the Programma Nazionale di Ricerche in Antartide, the Institut Polaire Français Paul Emile Victor (IPEV), and the Office of Polar Programs at the National Science Foundation (NSF). We thank Karim Agabi (University of Nice), Eric Aristidi (University of Nice), Tony Travouillon (University of New South Wales), and W. Lance Roth (University of Idaho) for launching radiosondes at Dome C. This project was supported by NSF grants OPP-97-26676 and ATM-98-13671.

Correspondence should be sent to P. M. Rowe at 1515 North Prospect Street, Tacoma, Washington 98406.

References

1. B. Soden, S. Tjemkes, J. Schmetz, R. Saunders, J. Bates, B. Ellingson, R. Engelen, L. Garand, D. Jackson, G. Jedlovec, T. Kleespies, D. Randel, P. Rayer, E. Salathe, D. Schwarzkopf, N. Scott, B. Sohn, S. de Souza-Machado, L. Strow, D. Tobin, D. Turner, P. van Delst, and T. Wehr, "An intercomparison of radiation codes for retrieving upper-tropospheric humidity in the 6.3-μm band: a report from the first GVAP workshop," Bull. Am. Meteorol. Soc. **81,** 797–808 (2000).
2. M. A. Ringer, J. M. Edwards, and A. Slingo, "Simulation of satellite channel radiances in the Met Office Unified Model," Q. J. R. Meteorol. Soc. **129,** 1169–1190 (2003).
3. Q. Ma and R. H. Tipping, "The density matrix of H_2O-N_2 in the coordinate representation: a Monte Carlo calculation of the far-wing lineshape," J. Chem. Phys. **112,** 574–584 (2000).
4. S. A. Clough, F. X. Kneizys, R. W. Davies, R. Gamache, and R. Tipping, "Theoretical line shape for H_2O vapor: application to the continuum," in *Atmospheric Water Vapor,* A. Deepak, T. D. Wilkerson, and L. H. Ruhnke, eds. (Academic, 1980), pp. 25–46.
5. D. E. Burch, D. A. Gryvnak, and R. R. Patty, "Absorption of infrared radiation by CO_2 and H_2O. Experimental techniques," J. Opt. Soc. Am. **57,** 885–895 (1967).
6. D. E. Burch, "Continuum absorption by H_2O," Rep. AFGL-TR-81-0300 (U.S. Air Force Geophysics Laboratory, Hanscom Air Force Base, Mass., 1982).
7. D. E. Burch and R. L. Alt, "Continuum absorption by H_2O in the 700–1200 cm^{-1} windows," Rep. AFGL-TR-84-0128 (U.S. Air Force Geophysics Laboratory, Hanscom Air Force Base, Mass., 1984).
8. D. C. Tobin, F. A. Best, P. D. Brown, S. A. Clough, R. G. Dedecker, R. G. Ellingson, R. K. Garcia, H. B. Howell, R. O. Knuteson, E. J. Mlawer, H. E. Revercomb, J. F. Short, P. F. W. van Deist, and V. P. Walden, "Downwelling spectral radiance observations at the SHEBA Ice Station: water vapor continuum measurements from 17 to 26 μm," J. Geophys. Res. **104,** 2081–2092 (1999).
9. D. E. Burch, D. A. Gryvnak, and F. J. Gates, "Continuum absorption by H_2O between 300 and 825 cm^{-1}," Rep. AFCRL-TR-740377 (U.S. Air Force Cambridge Research Laboratory, Bedford, Mass., 1974).
10. D. C. Tobin, L. L. Strow, W. J. Lafferty, and W. B. Olson, "Experimental investigation of the self- and N_2-broadened continuum within the ν_2 band of water vapor," Appl. Opt. **35,** 4724–4734 (1996).
11. Y. Han, J. A. Shaw, J. H. Churnside, P. D. Brown, and S. A. Clough, "Infrared spectral measurements in the tropical Pacific atmosphere," J. Geophys. Res. **102,** 4353–4356 (1997).
12. D. D. Turner, D. C. Tobin, S. A. Clough, P. D. Brown, R. G. Ellingson, E. J. Mlawer, R. O. Knuteson, H. E. Revercomb, T. R. Shippert, W. L. Smith, and M. W. Shephard, "The QME AERI LBLRTM: a closure experiment for downwelling high spectral resolution infrared radiance," J. Atmos. Sci. **61,** 2657–2675 (2004).
13. J. M. Theriault, P. L. Roney, D. St. Germain, H. E. Revercomb, R. O. Knuteson, and W. L. Smith, "Analysis of the FASCODE model and its H_2O continuum based on long-path atmospheric

transmission measurements in the 4.5–11.5 μm region," Appl. Opt. **33,** 323–333 (1994).
14. V. P. Walden, S. G. Warren, J. D. Spinhirne, A. Heymsfield, R. E. Brandt, P. Rowe, M. S. Town, S. Hudson, and R. M. Jones, "The South Pole Atmospheric Radiation and Cloud Lidar Experiment (SPARCLE)," in *Proceedings of the Sixth Conference on Polar Meteorology and Oceanography* (American Meteorological Society, 2001), pp. 297–299.
15. V. P. Walden, M. S. Town, B. Halter, and J. W. V. Storey, "First measurements of the infrared sky brightness at Dome C, Antarctica," Publ. Astron. Soc. Pac. **117,** 300–308 (2005).
16. E. Aristidi, K. Agabi, E. Fossat, J. Vernin, T. Travouillon, J. S. Lawrence, C. Meyer, J. W. V. Storey, B. Halter, W. L. Roth, and V. Walden, "An analysis of temperatures and wind speeds above Dome C, Antarctica," Astron. Astrophys. **430,** 739–746 (2005).
17. S. A. Clough, F. X. Kneizys, and R. W. Davies, "Line shape and the water vapor continuum," Atmos. Res. **23,** 229–241 (1989).
18. R. O. Knuteson, H. E. Revercomb, F. A. Best, N. C. Ciganovich, R. G. Dedecker, T. P. Dirkx, S. C. Ellington, W. F. Feltz, R. K. Garcia, H. B. Howell, W. L. Smith, J. F. Short, and D. C. Tobin, "Atmospheric Emitted Radiance Interferometer. Part I: Instrument design," J. Atmos. Oceanic Technol. **21,** 1763–1776 (2004).
19. R. O. Knuteson, H. E. Revercomb, F. A. Best, N. C. Ciganovich, R. G. Dedecker, T. P. Dirkx, S. C. Ellington, W. F. Feltz, R. K. Garcia, H. B. Howell, W. L. Smith, J. F. Short, and D. C. Tobin, "Atmospheric Emitted Radiance Interferometer. Part II: Instrument performance," J. Atmos. Oceanic Technol. **21,** 1777–1789 (2004).
20. Vaisala, http://www.vaisala.com/businessareas/measurementsystems/soundings/products/radiosondes/vaisalaradiosonders80.
21. S. R. Hudson, M. S. Town, V. P. Walden, and S. G. Warren, "Temperature, humidity, and pressure response of radiosondes at low temperatures," J. Atmos. Oceanic Technol. 825–836 (2004).
22. A. Jensen, "Correction of radiosonde measurements for lag error," Geophysica **6,** 275–279 (1958).
23. S. Twomey, *Introduction to the Mathematics of Inversion in Remote Sensing and Indirect Measurements* (Elsevier, 1977).
24. P. M. Rowe, "Measurements of the foreign-broadened continuum of water vapor in the 6.3 micron band at −30 Celsius," Ph.D. dissertation (University of Washington, Seattle, 2004).
25. V. P. Walden, S. G. Warren, and F. J. Murcray, "Measurements of the downward longwave radiation spectrum over the Antarctic plateau and comparisons to a line-by-line radiative transfer model for clear skies," J. Geophys. Res. **103,** 3825–3846 (1998), and references therein.
26. R. A. McClatchey, R. W. Fenn, J. E. A. Selby, F. E. Volz, and J. S. Garing, "Optical properties of the atmosphere," 3rd ed. AFCRL-72-0497 (U.S. Air Force Cambridge Research Laboratory, Bedford, Mass., 1972), p. 108.
27. S. A. Clough, M. W. Shephard, E. J. Mlawer, J. S. Delamere, M. J. Iacono, K. Cady-Pereira, S. Boukabara, and P. D. Brown, "Atmospheric radiative transfer modeling: a summary of the AER codes. Short communication," J. Quant. Spectrosc. Radiat. Transfer **91,** 233–244 (2005).
28. R. A. McClatchey, W. S. Benedict, S. A. Clough, D. E. Burch, R. F. Calfee, K. Fox, L. S. Rothman, and J. S. Garing, "AFCRL atmospheric absorption line parameters compilation," Rep. AFCRL-TR-730096 (Air Force Cambridge Research Laboratories, Bedford, Mass., 1973).
29. L. S. Rothman, R. R. Gamache, A. Goldman, L. R. Brown, R. A. Toth, H. M. Pickett, R. L. Poynter, J.-M. Flaud, C. Camy-Peyret, N. Husson, C. P. Rinsland, and M. A. H. Smith, "The HITRAN database: 1986 edition," Appl. Opt. **26,** 4058–4097 (1987).
30. L. S. Rothman, C. P. Rinsland, A. Goldman, S. T. Massie, D. P. Edwards, J.-M. Flaud, A. Perrin, C. Camy-Peyret, V. Dana, J.-Y. Mandin, J. Schroeder, A. McCann, R. R. Gamache, R. B. Wattson, K. Yashino, K. V. Chance, K. W. Jucks, L. R. Brown, N. Nemtchinov, and P. Varanasi, "The HITRAN molecular spectroscopic database and HAWKS (HITRAN Atmospheric Workstation): 1996 edition," J. Quant. Spectrosc. Radiat. Transfer **60,** 665–710 (1998).
31. L. S. Rothman, A. Barbe, D. C. Benner, L. R. Brown, C. Camy-Peyret, M. R. Carleer, K. Chance, C. Clerbaux, V. Dana, V. M. Devi, A. Fayt, J. M. Flaud, R. R. Gamache, A. Goldman, D. Jacquemart, K. W. Jucks, W. J. Lafferty, J. Y. Mandin, S. T. Massie, V. Nemtchinov, D. A. Newnham, A. Perrin, C. P. Rinsland, J. Schroeder, K. M. Smith, M. A. H. Smith, K. Tang, R. A. Toth, J. V. Auwera, P. Varanasi, and K. Yoshino, "The HITRAN molecular spectroscopic database: edition of 2000 including updates of 2001," J. Quant. Spectrosc. Radiat. Transfer **82,** 5–44 (2003).
32. E. J. Mlawer, S. A. Clough, and D. C. Tobin, "The MT_CKD water vapor continuum: a revised perspective including collision induced effects," presented at the Atmospheric Science from Space using Fourier Transform Spectrometry (ASSFTS) Workshop, Bad Wildbad (Black Forest), Germany, 8–10 October 2003.
33. P. R. Bevington and D. K. Robinson, *Data Reduction and Error Analysis for the Physical Sciences* (McGraw-Hill, 2003).
34. H. E. Revercomb, H. Buijs, H. B. Howell, D. D. LaPorte, W. L. Smith, and L. A. Sromovsky, "Radiometric calibration of IR Fourier transform spectrometers: solution to a problem with the High-Resolution Interferometer Sounder," Appl. Opt. **27,** 3210–3218 (1988).
35. L. S. Rothman, Harvard-Smithsonian Center for Astrophysics, Atomic and Molecular Physics Division, Cambridge, Mass. 02138 (personal communication, 2004).
36. S. A. Clough, Radiation & Climate Group, Atmospheric and Environmental Research, 131 Hartwell Ave., Lexington, Mass. 02421 (personal communication, 2004).
37. NOAA CMDL, http://www.cmdl.noaa.gov.
38. E. J. Dlugokencky, B. P. Walter, K. A. Masarie, P. M. Lang, and E. Kasischke, "Measurements of an anomalous global methane increase during 1998," Geophys. Res. Lett. **28,** 499–502 (2001).
39. T. J. Conway, P. P. Tans, L. S. Waterman, K. W. Thoning, D. R. Kitzis, K. A. Masarie, and N. Zhang, "Evidence for interannual variability of the carbon cycle from the NOAA/CMDL global air sampling network," J. Geophys. Res. **99,** 22831–22855 (1994).
40. P. C. Novelli, J. E. Elkins, and L. P. Steele, "The development and evaluation of a gravimetric reference scale for measurements of atmospheric carbon monoxide," J. Geophys. Res. **96,** 13109–13121 (1991).
41. P. R. Griffiths and J. A. deHaseth, *Fourier Transform Infrared Spectrometry* (Wiley, 1986).
42. M. C. Abrams, G. C. Toon, and R. A. Schindler, "Practical example of the correction of Fourier-transform spectra for detector nonlinearity," Appl. Opt. **33,** 6307–6314 (1994).